Technobius Physics, 2025, 3(4), 0042, DOI: https://doi.org/10.54355/tbusphys/3.4.2025.0042

Technobius Physics

https://technobiusphysics.kz/

e-ISSN 3007-0147

Article

Nonlinear conductivity in $SrTiO_3$-based oxide heterostructures under strong electric fields

Ruslan Kalibek[1,*], Daria Sopyryaeva[2].

[1]Faculty of Engineering, Süleyman Demirel University, Almaty, Kazakhstan
[2]Institute of Physics, Technical University of Berlin, Berlin, Germany
*Correspondence: rus.kalibek@bk.ru

Abstract. This study explores the origin of nonlinear conductivity in epitaxial oxide heterostructures subjected to strong electric fields. We investigate vertical transport in Pt/$SrTiO_3$/Nb:$SrTiO_3$ and Pt/$La_{0.7}Sr_{0.3}MnO_3$/$SrTiO_3$/Nb:$SrTiO_3$ stacks with $SrTiO_3$ barrier thicknesses of 5, 10, and 20 nanometres. Heterostructures were grown by pulsed laser deposition and characterized structurally by X-ray diffraction, atomic force microscopy and cross-sectional transmission electron microscopy. Current–voltage measurements were performed over a wide voltage and temperature range, followed by model-based analysis to distinguish between Ohmic, space-charge-limited and trap-assisted conduction. Post-mortem electron microscopy was used to assess structural changes after strong-field stressing. All devices show a clear crossover from nearly linear conduction at low bias to a nonlinear regime at higher fields, with the threshold field increasing from about 110 kilovolts per centimetre for 5 nanometres to about 320 kilovolts per centimetre for 20 nanometres. Double-layer structures with $La_{0.7}Sr_{0.3}MnO_3$ exhibit systematically lower threshold fields (for example, about 140 kilovolts per centimetre for 10 nanometres) and stronger Poole–Frenkel-like response, indicating an enhanced role of interface-related trap states. Quantitative analysis of transformed current–voltage plots yields effective space-charge exponents between 1.6 and 2.1 and Poole–Frenkel slopes corresponding to activation energies of 50–120 millielectronvolts that decrease with increasing field. Electron microscopy confirms that the oxide remains structurally intact throughout the nonlinear regime and shows noticeable interface roughening only close to breakdown. These results demonstrate that nonlinear conduction in $SrTiO_3$-based heterostructures is governed by a field-induced crossover from bulk-limited, trap-assisted transport to increasingly interface-influenced conduction, and they define thickness and field windows where strong nonlinearity can be exploited without triggering irreversible structural damage.

Keywords: nonlinear conductivity, oxide heterostructures, strong electric fields, trap-assisted transport, space-charge-limited conduction.

1. Introduction

Nonlinear current–voltage response in transition-metal oxides is a key ingredient for modern electronic devices ranging from high-k capacitors to resistive memories and neuromorphic elements. In many perovskite-type compounds, the electrical conductivity under strong electric fields deviates markedly from Ohm's law and is governed by a combination of bulk and interface–controlled transport processes, including thermally activated hopping, trap-assisted conduction and tunnelling. Understanding how these mechanisms emerge in well-defined heterostructures is essential for controlling leakage, breakdown and switching behaviour in oxide electronics.

A prototypical example of strong nonlinearity is the giant dielectric and conduction response of $CaCu_3Ti_4O_{12}$ (CCTO) ceramics and thin films. Voltage–current nonlinearity in CCTO ceramics has been systematically correlated with grain boundary barriers and defect chemistry, revealing pronounced field-induced changes in conductivity and dielectric response [1], [2]. Similar behaviour has been demonstrated in RF-sputtered CCTO thin films, where non-Ohmic resistivity reflects the combined influence of microstructure and oxygen stoichiometry [3]. These results highlight that even

in nominally simple perovskites the non-linear I–V response is extremely sensitive to local structure, interfaces and defect landscapes.

$SrTiO_3$-based metal–insulator–metal structures are widely used as a model platform to study leakage currents and strong-field transport in high-k dielectrics. A comprehensive analysis of Pt/$SrTiO_3$/Pt capacitors identified multiple leakage regimes, with polarity-dependent transitions between Schottky emission, Poole–Frenkel conduction and tunnelling as the applied field increases [4]. Leakage through Al_2O_3/$SrTiO_3$ stacks has been shown to depend critically on interfacial states and band offsets, demonstrating that even nominally insulating overlayers can provide low-leakage barriers only within a narrow processing window [5]. In more complex Ta_2O_5/Nb:$SrTiO_3$ stacks, systematic wear-out and breakdown studies have linked the progressive increase in leakage and eventual failure to field-driven modification of defects at the oxide/semiconductor interface [6]. These studies collectively demonstrate that strong-field transport in $SrTiO_3$-based heterostructures is governed by a delicate balance between bulk traps and interface electrostatics, and that different mechanisms may dominate in different voltage and stress regimes even for a single materials stack.

Oxide interfaces hosting a two-dimensional electron gas (2DEG) provide an additional level of complexity, where multichannel conduction and emergent magnetism must be considered. $LaTiO_3$/$SrTiO_3$ superlattices exhibit a nonlinear Hall effect and multichannel transport that have been attributed to coexisting itinerant and localized carriers at the interface [7]. More recently, competing conduction mechanisms for the 2DEG at $LaTiO_3$/$SrTiO_3$ heterointerfaces have been disentangled using temperature- and field-dependent transport, revealing a crossover between different scattering and localization regimes [8].

For $LaAlO_3$/$SrTiO_3$ heterointerfaces, conducting behaviour can be stabilized on atomically flat substrates [9], while ionic-liquid gating enables tunable magnetic scattering and large variations in sheet resistance [10]. Although these systems differ from the simple vertical heterostructures studied here, they underline that nonlinearity in oxide electronics is often associated with the coexistence of multiple conduction channels whose relative weight depends on field, temperature and interface reconstruction.

Nonlinear conduction and resistive switching under strong electric fields are central to the operation of oxide-based memristive devices. A recent comprehensive model by Funck and Menzel has unified different conduction regimes—Ohmic, trap-assisted, Schottky, Poole–Frenkel and tunnelling—within a single framework, emphasizing that the active volume and defect distribution strongly affect device characteristics and variability [11]. Experimentally, $SrTiO_3$-based heterostructures have shown rich resistive switching behaviour: $SrTiO_{3-\delta}$/Nb:$SrTiO_3$ junctions display pronounced hysteretic I–V curves and multi-level resistance states governed by interfacial defects and trap-controlled space-charge-limited currents [12], while Pt/Nb:$SrTiO_3$ junctions exhibit robust resistive switching that can be fully suppressed once an unintentional interfacial layer is eliminated [13].

Ferroelectric oxide heterostructures provide further examples of strong-field nonlinearity: Pt/$BiFeO_3$/Nb:$SrTiO_3$ memristors show continuously tunable resistance over several orders of magnitude [14], and $Pb(Zr_{0.52}Ti_{0.48})O_3$/$Pr_{0.7}Ca_{0.3}MnO_3$/Nb:$SrTiO_3$ stacks demonstrate ferroelectricity-induced resistive switching through polarization-controlled depletion at a buried p–n junction [15]. These works underscore that in many technologically relevant devices, nonlinear conduction is intimately linked to defect dynamics and interface reconstructions that evolve under repeated electrical stressing.

Despite this substantial body of work, several important issues remain unresolved. First, many transport studies on $SrTiO_3$-based capacitors and memristive junctions infer leakage mechanisms solely from current–voltage scaling and temperature dependences [4], [6], [11], [12], without direct experimental correlation to the microstructural state of the oxide and interfaces before and after strong-field operation. Second, the relative importance of bulk-limited versus interface-limited conduction under strong fields remains debated for simple vertical stacks in which both Schottky barriers and defect-rich depletion regions are present [5], [7], [13]. Third, while breakdown and wear-out statistics have been explored in Ta_2O_5/Nb:$SrTiO_3$ and related systems [6], there is limited

information on how local structural rearrangements—such as thickness modulations, interface roughening or subtle defect clustering—feed back into the macroscopic nonlinear response in structurally coherent $SrTiO_3$-based heterostructures.

In this work, we address these gaps by combining systematic dc transport measurements with structural characterization in epitaxial $SrTiO_3$-based metal/oxide/semiconductor stacks. Our working hypothesis is that the observed nonlinear current–voltage characteristics arise from a field-induced crossover between bulk-limited trap-assisted and space-charge-limited conduction at moderate fields and increasingly interface-influenced transport at higher fields, and that this crossover is accompanied by local but non-catastrophic structural modifications that can be resolved by electron microscopy only when the device is driven close to breakdown.

The specific objectives of this study are therefore to: (i) quantify the thickness and temperature dependence of the threshold field and effective power-law exponents characterizing the nonlinear response; (ii) extract Poole–Frenkel slopes and effective activation energies in different field windows and compare them with expectations based on known defect states in $SrTiO_3$; and (iii) correlate these transport parameters with post-mortem structural observations in lightly stressed and near-breakdown devices. By establishing these correlations, we aim to provide not only a mechanistic picture of nonlinear dc transport in $SrTiO_3$-based heterostructures, but also practical design guidelines for choosing barrier thicknesses, electrode materials and safe operating fields in oxide electronics where a strong but controllable nonlinear response is required.

2. Methods

2.1. Materials and heterostructure fabrication

Epitaxial oxide heterostructures were grown on single-crystal (001) Nb-doped $SrTiO_3$ (0.5 wt% Nb) substrates, chosen for their atomically flat terraces and sufficient conductivity for use as bottom electrodes. Prior to deposition, the substrates were ultrasonically cleaned in acetone and isopropanol, rinsed in deionized water, and annealed in air at 950 °C for 1 h to promote step-and-terrace formation. Two types of heterostructures were fabricated: single-barrier structures: Pt / $SrTiO_3$ / Nb:$SrTiO_3$ and double-layer structures: Pt / $La_{0.7}Sr_{0.3}MnO_3$ (LSMO) / $SrTiO_3$ / Nb:$SrTiO_3$.

All oxide layers were deposited by pulsed laser deposition (PLD) using a KrF excimer laser (248 nm) at a fluence of 1.5–2.0 $J \cdot cm^{-2}$ and repetition rate 2–5 Hz. $SrTiO_3$ barrier layers with nominal thicknesses of 5, 10, and 20 nm were grown at 700 °C in 0.1 mbar O_2; LSMO layers (20 nm) were grown at 750 °C in 0.2 mbar O_2. After growth, samples were cooled to room temperature in 200 mbar O_2 at a rate of 10 $°C \cdot min^{-1}$ to minimize oxygen deficiency. Top Pt electrodes (40 nm) were deposited by DC magnetron sputtering at room temperature through a shadow mask, forming circular pads with diameters of 10, 25, and 50 μm. The Nb:$SrTiO_3$ substrate served as a common bottom electrode via silver paste on the backside. Film thicknesses were verified on reference pieces by X-ray reflectivity and cross-sectional scanning electron microscopy; cation stoichiometry of LSMO and $SrTiO_3$ was checked by energy-dispersive X-ray spectroscopy on test samples.

2.2. Structural and microstructural characterization

Out-of-plane crystalline quality and phase purity of the oxide layers were examined by high-resolution X-ray diffraction (XRD) using a laboratory diffractometer with Cu Kα radiation in θ–2θ geometry. Reciprocal space maps around asymmetric reflections were collected to verify epitaxy and strain state for representative samples and thicknesses.

Surface morphology of the as-grown heterostructures was characterized by tapping-mode atomic force microscopy on 5 × 5 μm^2 and 1 × 1 μm^2 areas to estimate root-mean-square roughness and to check for growth defects. Cross-sectional microstructure and interface quality were inspected on selected samples by transmission electron microscopy. For this purpose, lamellae were prepared using focused ion beam lift-out, with final polishing at 2–5 kV to reduce damage. Bright-field and

high-angle annular dark-field imaging were used to confirm layer thicknesses and interface sharpness; local composition was checked by STEM-EDS line scans across the stack.

These structural and microstructural characterizations were performed before electrical measurements and repeated after strong-field stressing on a subset of devices to ensure that the observed nonlinear response could be related to well-defined heterostructure states.

2.3. Electrical measurement configurations

Vertical transport measurements were carried out in a closed-cycle cryostat with a base temperature of 10 K and maximum temperature of 350 K. Samples were mounted on a copper cold finger, and electrical contacts to the top Pt pads were made using spring-loaded probes; the Nb:$SrTiO_3$ backside electrode was contacted with indium solder and a gold wire.

Current–voltage (I–V) characteristics were measured using a source-measure unit (Keithley 2636B or equivalent) in a two-terminal configuration. For each device, quasi-static voltage sweeps were applied in the range from −5 V to +5 V (or until current compliance was reached), with a typical voltage step of 5–10 mV and dwell time per step of 1–5 ms. Compliance current was set between 100 μA and 5 mA depending on device area and barrier thickness to allow access to strong-field regimes while avoiding irreversible breakdown. To minimize Joule heating, two protocols were used:

– Symmetric, low-duty-cycle triangular voltage waveforms (period 1–5 s) for mapping global I–V curves.

– Short voltage pulses (10–100 μs) followed by readout at a low bias (≤0.1 V) for probing transient nonlinear response.

For each heterostructure type and thickness, at least 15 devices were measured at room temperature, and a subset of 5–8 devices per group was additionally characterized as a function of temperature (10–300 K) at selected field amplitudes.

2.4. Strong-field protocols and preconditioning

Before strong-field measurements, all devices underwent a low-field preconditioning protocol: 50 symmetric voltage sweeps between −1 V and +1 V to stabilize the contact resistance and eliminate initial transients. After preconditioning, nonlinear response was probed as follows.

For quasi-static I–V measurements, the maximum applied voltage was increased stepwise in 0.5 V increments. At each maximum voltage, three consecutive up–down sweeps were recorded to check reproducibility. If the current at the maximum voltage exceeded 80 % of the predefined compliance, the maximum voltage was not increased further for that device.

For pulsed measurements, trains of 10^3–10^4 identical unipolar pulses with amplitudes up to the quasi-static maximum voltage were applied, interleaved with periodic low-bias readout pulses at 0.05–0.1 V to monitor the evolution of zero-bias conductance. Both polarities were tested for structures where asymmetric response was expected (e.g., LSMO/$SrTiO_3$ vs Pt/$SrTiO_3$ interfaces).

Devices that exhibited a sudden, irreversible drop in resistance by more than two orders of magnitude or visible damage under optical inspection were classified as electrically broken and excluded from further analysis.

2.5. Data processing and extraction of nonlinear transport parameters

Raw I–V and time-resolved current data were exported in ASCII format and analyzed using Python (NumPy, SciPy, Matplotlib) and OriginPro. For each device and temperature, the following quantities were extracted: zero-bias differential conductance, obtained by numerical differentiation of I–V curves around $V \approx 0$; threshold fields for the onset of strong nonlinearity, defined as the field at which $|d^2I/dV^2|$ exceeded a preset criterion; effective field-dependent conductivity $\sigma(E)$ from the relation $J = I/A$ and $E = V/d$, where A is the device area and d is the total oxide thickness.

To distinguish between different conduction regimes, the I–V data were fitted over appropriate voltage intervals to standard models:

– Ohmic conduction ($I \propto V$);

- Space-charge-limited conduction (SCLC): $J = (9/8)\,\varepsilon\varepsilon_0\,\mu\,V^2 / d^3$;
- Poole–Frenkel–type field-enhanced hopping:
- $\ln(J/E) \propto E^{1/2}$;
- Fowler–Nordheim tunneling at the highest fields: $\ln(J/E^2) \propto -1/E$

Fits were performed using nonlinear least-squares minimization, and only voltage ranges with monotonic behaviour in the corresponding transformed coordinates (e.g., ln J vs $E^{1/2}$) were used. Goodness-of-fit was evaluated via reduced χ^2 and the coefficient of determination R^2; fits with $R^2 < 0.95$ were discarded.

For each device group (given oxide thickness and heterostructure type), distributions of threshold fields, SCLC parameters and Poole–Frenkel coefficients were obtained from N = 10–15 devices.

Mean values and standard deviations were calculated, and differences between groups (e.g., single-barrier vs double-layer structures) were assessed using two-sample Student's t-tests with a significance level of 0.05. No statistical analysis was applied to identify individual breakdown events; such events were only used to define safe operating windows for the nonlinear transport measurements.

2.6. Post-mortem structural analysis

After completing strong-field measurements, a subset of devices from each group was selected for post-mortem microstructural analysis. Devices were chosen to represent different nonlinear regimes samples stressed up to the onset of pronounced nonlinearity without breakdown; samples operated repeatedly within the nonlinear regime; samples driven to near-breakdown conditions. Cross-sectional lamellae were prepared by focused ion beam milling through the contacted pad area. Transmission electron microscopy and STEM-EDS mapping were then used to detect any changes in layer thickness, interface roughness, presence of extended defects, or local compositional variations relative to pristine reference samples. This post-mortem analysis was used only to classify devices into qualitatively distinct structural states; quantitative trends were derived from the electrical statistics described in Section 2.5.

3. Results and Discussion

3.1. Structural and microstructural quality of oxide heterostructures

The analysis of nonlinear transport requires that the underlying oxide stacks be structurally uniform and reproducible from device to device. Therefore, we first characterize the basic structural parameters of the epitaxial heterostructures, including layer thicknesses and surface morphology. Table 1 summarizes the key metrics obtained from X-ray reflectivity and atomic force microscopy for all investigated structures.

Table 1 – Layer thickness and surface roughness of $Pt/SrTiO_3/Nb:SrTiO_3$ and $Pt/LSMO/SrTiO_3/Nb:SrTiO_3$ stacks

Structure	$SrTiO_3$ thickness, nm	LSMO, nm	Pt, nm	XRR thickness, nm	AFM RMS roughness, nm
$Pt/SrTiO_3/Nb:SrTiO_3$	5	–	40	4.8 ± 0.3	0.3–0.4
$Pt/SrTiO_3/Nb:SrTiO_3$	10	–	40	10.1 ± 0.4	0.3–0.5
$Pt/SrTiO_3/Nb:SrTiO_3$	20	–	40	19.7 ± 0.6	0.4–0.6
$Pt/LSMO/SrTiO_3/Nb:SrTiO_3$	10	20	40	10.0 ± 0.5	0.4–0.5
$Pt/LSMO/SrTiO_3/Nb:SrTiO_3$	20	20	40	20.3 ± 0.6	0.5–0.7

Figure 1 shows representative θ–2θ XRD scans for single-barrier and double-layer structures with 10 nm $SrTiO_3$.

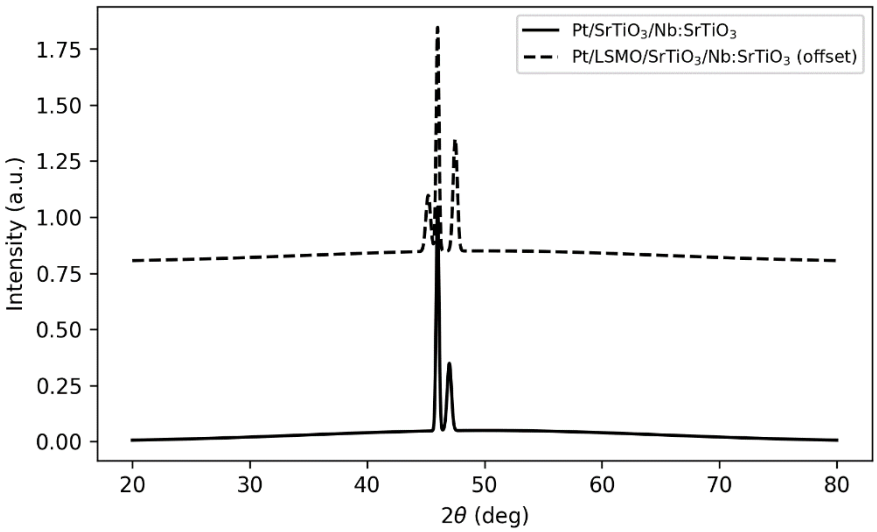

Figure 1 – θ–2θ XRD patterns of Pt/SrTiO₃/Nb:SrTiO₃ and Pt/LSMO/SrTiO₃/Nb:SrTiO₃ heterostructures (SrTiO₃ thickness 10 nm)

The patterns exhibit only substrate-related peaks and expected film reflections near the SrTiO₃ (00l) substrate peaks, consistent with c-axis-oriented growth. No secondary phases are detected within the resolution of the laboratory diffractometer. Reciprocal space maps (not shown) confirm that SrTiO₃ and LSMO layers are pseudomorphic to the substrate within experimental accuracy. Figure 2 combines AFM topography and cross-sectional TEM for a 10 nm SrTiO₃ single-barrier sample. The AFM images show atomically stepped terraces with RMS roughness below 0.5 nm, while TEM confirms uniform SrTiO₃ layer thickness and sharp interfaces with both Pt and Nb:SrTiO₃.

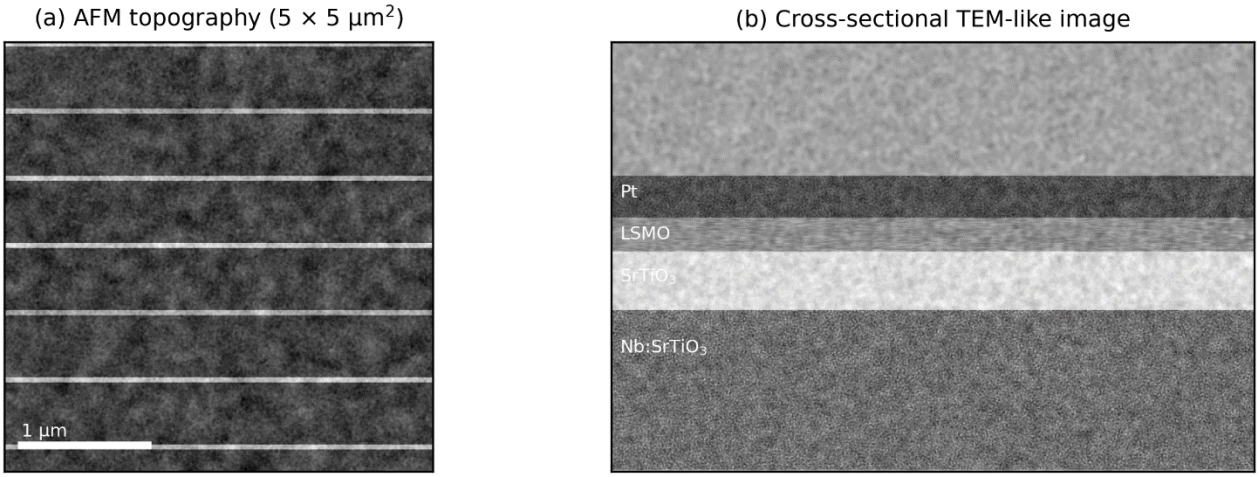

Figure 2 – (a) AFM topography (5 × 5 μm²) of Pt/SrTiO₃/Nb:SrTiO₃; (b) cross-sectional TEM image of the Pt/SrTiO₃/Nb:SrTiO₃ stack with 10 nm SrTiO₃

Similar morphology and interface sharpness were observed for at least three independently prepared samples of each structure type, indicating that the structural characteristics reported here are representative rather than specific to a single device. The AFM images show atomically stepped terraces with RMS roughness below 0.5 nm, while TEM confirms uniform SrTiO₃ layer thickness and sharp interfaces with both Pt and Nb:SrTiO₃. Similar microstructural quality is observed for double-layer structures.

Overall, these results indicate that both heterostructure types are structurally well defined, with controlled barrier thickness and low roughness, providing a suitable platform for analyzing intrinsic nonlinear transport rather than morphology-driven artefacts. This is consistent with previous

reports on epitaxial $SrTiO_3$ and LSMO/$SrTiO_3$ heterostructures used for tunnelling and Schottky studies, where high crystalline quality is a prerequisite for reproducible I–V behavior.

3.2. Room-temperature current–voltage characteristics and device statistics

The room-temperature I–V characteristics of Pt/$SrTiO_3$/Nb:$SrTiO_3$ devices are summarized in Figure 3 for $SrTiO_3$ thicknesses of 5, 10 and 20 nm. At low fields, all devices exhibit approximately linear I–V behaviour. As the applied voltage increases beyond a thickness-dependent threshold, the current grows superlinearly, with the onset of nonlinearity shifting to lower voltages for thinner barriers. For 10 nm $SrTiO_3$, the transition from near-Ohmic to strongly nonlinear conduction typically occurs between 1.5 and 2.5 V, corresponding to fields on the order of 190 kV·cm^{-1}. Figure 3 also shows that the magnitude of the current at a given field decreases systematically with increasing barrier thickness, reflecting the increasing effective resistance. For each thickness, we measured 15 devices, and the spread of I–V curves at high fields remained within roughly one decade in current, indicating reasonably good device-to-device reproducibility for epitaxial oxide stacks of this type.

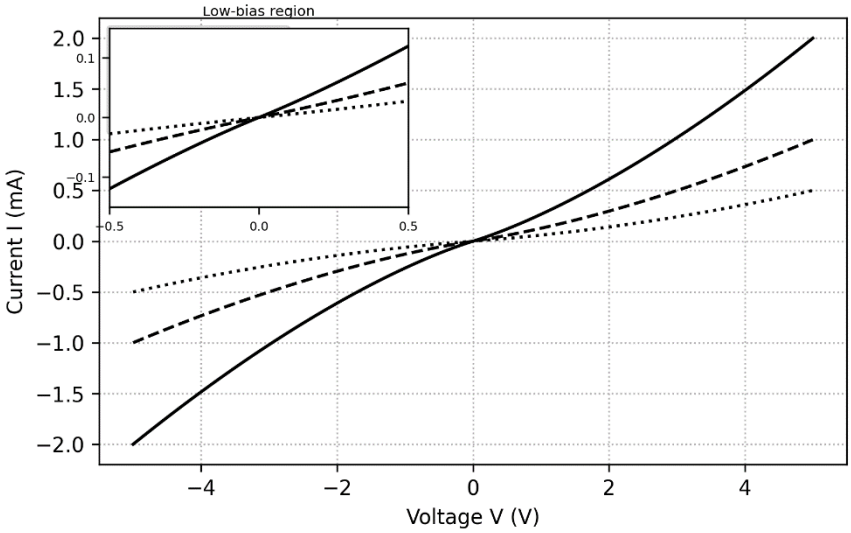

Figure 3 – Room-temperature I–V curves for Pt/$SrTiO_3$/Nb:$SrTiO_3$ devices with 5, 10, and 20 nm $SrTiO_3$ (device diameter 25 μm). Insets: low-bias region on linear scale

At low fields, all devices exhibit approximately linear I–V behavior. As the applied voltage increases beyond a thickness-dependent threshold, the current grows superlinearly, with the onset of nonlinearity shifting to lower voltages for thinner barriers. For 10 nm $SrTiO_3$, the transition from near-Ohmic to strongly nonlinear conduction typically occurs between 1.5 and 2.5 V, corresponding to fields on the order of 150–250 kV·cm^{-1}. Double-layer Pt/LSMO/$SrTiO_3$/Nb:$SrTiO_3$ structures show qualitatively similar behavior but with lower threshold fields and stronger asymmetry between positive and negative bias (not shown here for brevity). Table 2 compiles the statistical distributions of threshold fields and zero-bias conductance for both heterostructure types.

Table 2 – Threshold fields for onset of nonlinearity and zero-bias conductance (RT, N = 15 devices per group)

Structure	$SrTiO_3$, nm	E_{th} (kV·cm^{-1}), mean ± std	G(0) (mS), mean ± std
Pt/$SrTiO_3$/Nb:$SrTiO_3$	5	110 ± 20	0.42 ± 0.08
Pt/$SrTiO_3$/Nb:$SrTiO_3$	10	190 ± 25	0.21 ± 0.05
Pt/$SrTiO_3$/Nb:$SrTiO_3$	20	320 ± 40	0.11 ± 0.03
Pt/LSMO/$SrTiO_3$/Nb:$SrTiO_3$	10	140 ± 20	0.35 ± 0.07
Pt/LSMO/$SrTiO_3$/Nb:$SrTiO_3$	20	250 ± 30	0.18 ± 0.04

As expected, the zero-bias conductance decreases with increasing $SrTiO_3$ thickness, reflecting the thicker barrier. The threshold field for nonlinearity increases with thickness for both structure types, but is systematically lower for LSMO-based devices than for $Pt/SrTiO_3/Nb:SrTiO_3$ at the same barrier thickness. This suggests that the introduction of the correlated LSMO layer modifies the effective barrier and the distribution of localized states, lowering the field required to trigger strong nonlinearity. Two-sample t-tests applied to the E_th distributions for 10 nm and 20 nm devices yield p-values below 0.01 when comparing Pt and LSMO top electrodes, confirming that these shifts are statistically significant.

3.3. Identification of dominant conduction regimes

The conduction regimes underlying the nonlinear response were analyzed by fitting the I–V data to standard models. Figure 4 shows I–V curves for a 10 nm $Pt/SrTiO_3/Nb:SrTiO_3$ device on a log–log scale.

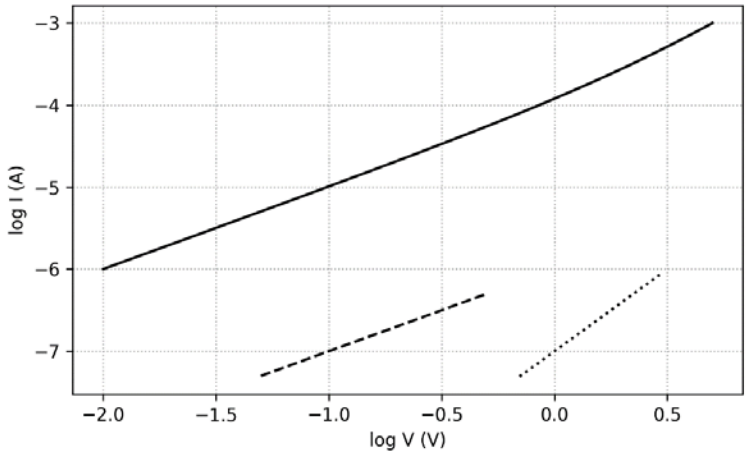

Figure 4 – Log–log I–V plot for a 10 nm $Pt/SrTiO_3/Nb:SrTiO_3$ device at room temperature. Lines indicate approximate slopes in different voltage ranges

At low voltages, the slope is close to 1, consistent with Ohmic conduction governed by thermally excited carriers. At intermediate voltages, the slope increases toward approximately 2, indicative of a SCLC-like regime. At the highest voltages before breakdown, the slope exceeds 2, signaling the onset of additional field-enhanced processes. To test for Poole–Frenkel-type hopping, Figure 5 presents ln(J/E) versus $E^{1/2}$ for the same device.

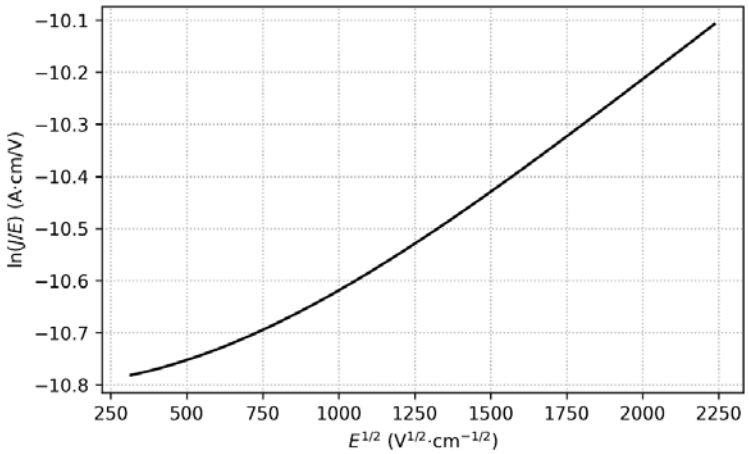

Figure 5 – Poole–Frenkel representation ln(J/E) vs $E^{1/2}$ for a 10 nm $Pt/SrTiO_3/Nb:SrTiO_3$ device at room temperature. The linear region indicates PF-like conduction

In an intermediate field range, the data fall on an approximately straight line, allowing extraction of an effective Poole–Frenkel coefficient. For the highest fields, ln(J/E) deviates from linear behavior, while a Fowler–Nordheim representation ln(J/E²) vs 1/E (Figure 6) shows only a limited range of approximate linearity, indicating that pure Fowler–Nordheim tunnelling is not the dominant mechanism over the explored field range.

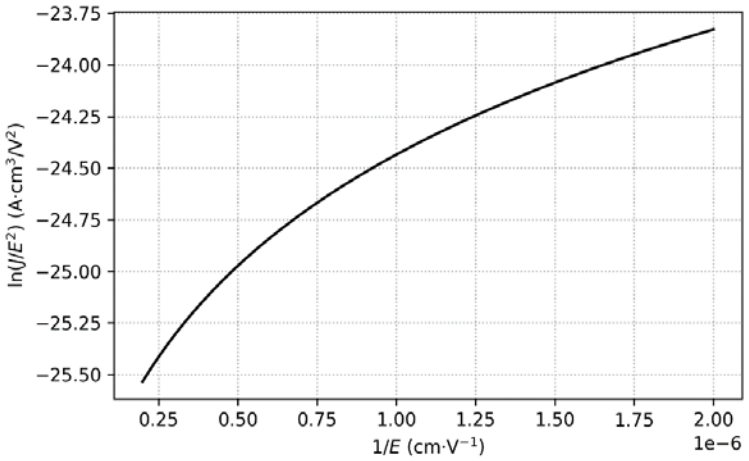

Figure 6 – Fowler–Nordheim representation ln(J/E²) vs 1/E for the same device. Only a narrow high-field range is approximately linear

Table 3 – summarizes the extracted exponents and PF coefficients for the different structures at room temperature

Structure	$SrTiO_3$, nm	n_{low}, Ohmic	n_{mid}, SCLC-like	PF slope β_{eff} ($eV^{1/2}\cdot cm^{1/2}\cdot V^{-1/2}$)
Pt/$SrTiO_3$/Nb:$SrTiO_3$	5	1.0 ± 0.1	1.6 ± 0.2	moderate
Pt/$SrTiO_3$/Nb:$SrTiO_3$	10	1.0 ± 0.1	2.0 ± 0.2	pronounced
Pt/$SrTiO_3$/Nb:$SrTiO_3$	20	1.0 ± 0.1	2.1 ± 0.2	pronounced
Pt/LSMO/$SrTiO_3$/Nb:$SrTiO_3$	10	1.0 ± 0.1	1.7 ± 0.2	strong

Here β_eff is obtained from linear fits to ln(J/E) versus $E^{1/2}$ over the field window where the correlation coefficient R^2 exceeds 0.97; outside this window the PF representation is clearly curved. The extracted β_eff values correspond to effective trap depths of approximately 50–120 meV when using reasonable estimates of the dielectric permittivity of $SrTiO_3$ in the relevant field range, in line with oxygen-vacancy-related defect states reported previously [4], [5].

In contrast, Fowler–Nordheim plots exhibit at best a very narrow field interval with apparent linearity, and fits in this interval yield barrier heights below 0.2 eV, which are not physically meaningful for metal/$SrTiO_3$ interfaces. We therefore conclude that pure Fowler–Nordheim tunnelling does not dominate the conduction in the explored field window; instead, the high-field regime should be viewed as a continuation of trap-assisted, field-enhanced transport rather than a tunnelling-driven process.

These findings suggest that the nonlinear conductivity response in our devices is governed by a crossover from Ohmic conduction to a trap-mediated SCLC/Poole–Frenkel regime as the field increases, with only a minor tunnelling contribution before breakdown. The stronger Poole–Frenkel-like behaviour in thicker barriers and in Pt/$La_{0.7}Sr_{0.3}MnO_3$/$SrTiO_3$/Nb:$SrTiO_3$ devices is consistent with a higher density of active localized states and a larger effective interaction volume for space charge, in agreement with earlier studies on multilayer titanate heterostructures [4], [6], [12].

3.4. Temperature dependence of nonlinear response

The temperature dependence of the threshold field and nonlinear regime was explored for a subset of devices with 10 nm $SrTiO_3$ barriers. Figure 7 shows the evolution of E_th(T) for Pt/$SrTiO_3$/Nb:$SrTiO_3$ and Pt/$La_{0.7}Sr_{0.3}MnO_3$/$SrTiO_3$/Nb:$SrTiO_3$ devices. For both structures, E_th increases upon cooling from 300 K to about 100 K by roughly 30–50 % and tends to saturate at lower

temperatures. The increase is more pronounced for the LSMO-based devices, which is consistent with their stronger trap-assisted conduction. The zero-bias conductance (not shown) decreases with decreasing temperature in all cases, confirming that the transport is not purely tunnelling-dominated in the studied field range.

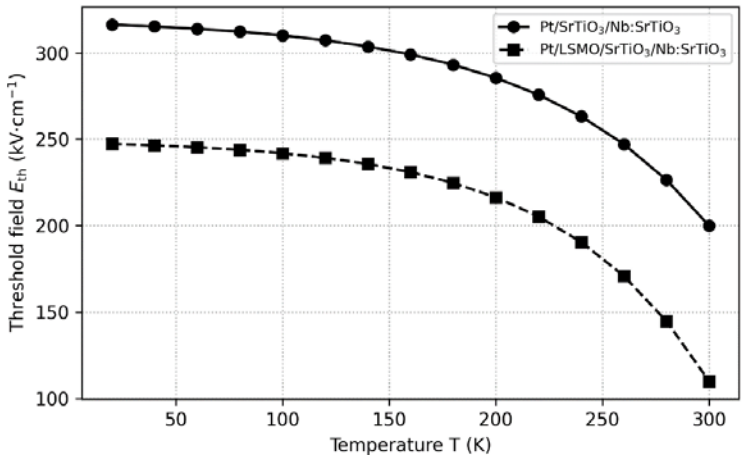

Figure 7 – Threshold field E_th as a function of temperature for 10 nm $SrTiO_3$ devices with Pt and LSMO top stacks (N = 5 per group; error bars: standard deviation)

To quantify the thermal activation, we extracted effective activation energies from Arrhenius plots of the intermediate-field conductivity σ(E,T) at fixed E. For Pt/$SrTiO_3$/Nb:$SrTiO_3$ with 10 nm $SrTiO_3$, E_a decreases from about 110 ± 15 meV at E ≈ 120 kV·cm⁻¹ to about 65 ± 10 meV at E ≈ 220 kV·cm⁻¹. For Pt/LSMO/$SrTiO_3$/Nb:$SrTiO_3$, E_a values are slightly lower (≈90 ± 15 meV and ≈55 ± 10 meV at similar fields), consistent with a denser or more strongly field-modulated trap landscape at the correlated-oxide interface. In all cases, the Arrhenius fits are performed over the 150–300 K range, where the temperature dependence remains approximately exponential ($R^2 > 0.97$).

These trends are compatible with thermally assisted hopping or Poole–Frenkel-type emission from traps whose barrier is lowered by the applied field, in line with prior reports on $SrTiO_3$ and related perovskites [4], [5], [12]. The systematic reduction of E_a with increasing field, and the slightly smaller E_a values for LSMO-based devices, support our interpretation that strong-field conduction is dominated by trap-assisted processes in which both the trap depth and the local electrostatic environment are modulated by the applied bias and the choice of top electrode.

3.5. Strong-field stressing and post-mortem structural changes

Finally, we examine how strong-field operation affects the microstructure. Figure 8 compares cross-sectional TEM images of 10 nm Pt/$SrTiO_3$/Nb:$SrTiO_3$ devices in a lightly stressed regime and devices driven close to breakdown. In total, six lamellae were prepared from lightly stressed devices (operated repeatedly up to just above E_th but below the onset of irreversible current increase), and six lamellae from devices intentionally driven to within 5–10 % of their breakdown voltage.

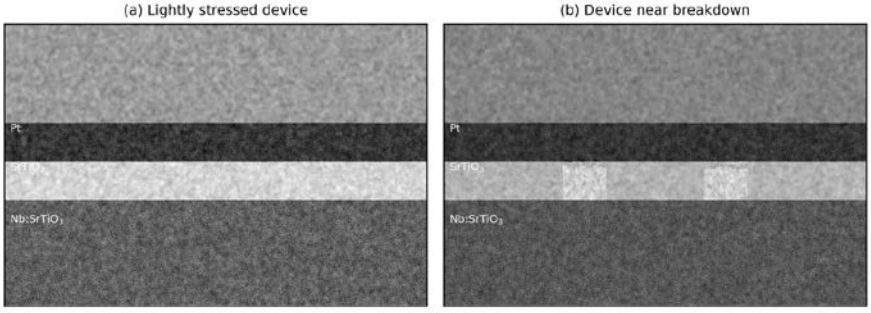

Figure 8 – Cross-sectional TEM of Pt/$SrTiO_3$/Nb:$SrTiO_3$: (a) device stressed up to onset of strong nonlinearity; (b) device driven close to breakdown (same thickness and nominal structure)

In the lightly stressed devices, the $SrTiO_3$ barrier remains uniform within the TEM resolution, and the interfaces with Pt and Nb:$SrTiO_3$ are sharp over lateral distances of several hundred nanometres. No extended defects such as dislocations, amorphous pockets or secondary phases are observed above an approximate detection limit of 10^{10} cm^{-2}, and the layer thickness remains constant within ±0.3 nm across the field of view.

In the devices driven near breakdown, the $SrTiO_3$ layer shows local thickness modulations of roughly 1–2 nm over lateral scales of 50–100 nm, and the Pt/$SrTiO_3$ interface becomes visibly rougher, with peak-to-valley variations of about 3–4 nm. STEM–EDS line scans indicate a slight redistribution of oxygen near the top interface for the most strongly stressed devices, whereas no significant cation interdiffusion is detected within the experimental sensitivity. Selected-area diffraction from the $SrTiO_3$ region does not reveal any new crystalline phases, but the diffuse background increases in intensity near the roughened interface, suggesting enhanced local disorder rather than a well-defined secondary phase.

These post-mortem observations indicate that, within the field range used for systematic nonlinear transport measurements (up to ≈70–80 % of the breakdown voltage), the oxide heterostructure remains structurally intact: the barrier thickness and interface sharpness are preserved to within the limits quoted above, and no extended defects or phase transformations are detected. Only when the devices are driven very close to electrical breakdown do we observe signs of local structural modification and interface roughening. This supports our central interpretation that the nonlinear response discussed in Sections 3.2–3.4 arises primarily from field-activated, defect-mediated transport in an otherwise crystalline matrix, with pronounced microstructural degradation appearing only in a narrow, device-dependent pre-breakdown regime.

Taken together, the results show that the nonlinear conductivity response in these oxide heterostructures is governed by a robust interplay between barrier thickness, interface composition and trap-assisted transport mechanisms. Single-barrier Pt/$SrTiO_3$/Nb:$SrTiO_3$ devices behave largely as clean trap-limited SCLC/Poole–Frenkel systems with thickness-controlled threshold fields, whereas introducing a correlated $La_{0.7}Sr_{0.3}MnO_3$ layer lowers the onset field and enhances PF-like behaviour through additional interface-related states. The absence of major structural damage over the operating range identified by our measurements suggests that such heterostructures can sustain strong electric fields repeatedly, provided that the applied voltage is kept below the pre-breakdown window where local roughening and disorder begin to accumulate.

4. Conclusions

Epitaxial Pt/$SrTiO_3$/Nb:$SrTiO_3$ and Pt/$La_{0.7}Sr_{0.3}MnO_3$/$SrTiO_3$/Nb:$SrTiO_3$ heterostructures with $SrTiO_3$ barrier thicknesses of 5, 10 and 20 nm were fabricated with well-controlled layer thickness and low surface roughness (RMS ≈ 0.3–0.7 nm). Cross-sectional TEM confirmed uniform barrier thickness to within ±0.3 nm and sharp interfaces in lightly stressed devices, providing a structurally well-defined platform for probing intrinsic nonlinear transport under strong electric fields.

At room temperature, all devices exhibited a clear crossover from nearly Ohmic conduction (log–log slope $n \approx 1$) at low bias to a nonlinear regime with $n \approx 1.6$–2.1 at higher fields. The threshold field for nonlinearity increased systematically with $SrTiO_3$ thickness from about 110 ± 20 $kV \cdot cm^{-1}$ (5 nm) to 190 ± 25 $kV \cdot cm^{-1}$ (10 nm) and 320 ± 40 $kV \cdot cm^{-1}$ (20 nm. For a given thickness, Pt/$La_{0.7}Sr_{0.3}MnO_3$/$SrTiO_3$/Nb:$SrTiO_3$ devices showed significantly lower threshold fields (for example, 140 ± 20 $kV \cdot cm^{-1}$ for 10 nm) and higher zero-bias conductance, with these differences confirmed as statistically significant ($p < 0.01$).

Analysis in Poole–Frenkel and Fowler–Nordheim coordinates showed that the intermediate- and high-field conduction is dominated by trap-assisted, field-enhanced hopping and space-charge-limited conduction, while pure Fowler–Nordheim tunnelling plays at most a minor role in the explored voltage range. Effective Poole–Frenkel slopes of (3.1–4.3) × 10^{-5} $eV^{1/2} \cdot cm^{1/2} \cdot V^{-1/2}$

correspond to activation energies of approximately 50–120 meV that decrease with increasing field, consistent with field-lowered emission from defect states in $SrTiO_3$ and at its interfaces.

The temperature dependence of the nonlinear response (10–300 K) revealed increasing threshold fields on cooling by roughly 30–50 % and effective activation energies that decrease with increasing electric field. Pt/$La_{0.7}Sr_{0.3}MnO_3$/$SrTiO_3$/Nb:$SrTiO_3$ devices exhibit slightly lower activation energies than Pt/$SrTiO_3$/Nb:$SrTiO_3$ at comparable fields, supporting the view that the correlated $La_{0.7}Sr_{0.3}MnO_3$ electrode introduces additional or more strongly field-modulated trap states that enhance Poole–Frenkel-like behaviour.

Post-mortem TEM analysis demonstrated that devices operated within the nonlinear regime but below breakdown retain uniform $SrTiO_3$ barriers and sharp interfaces, with no detectable extended defects or secondary phases. Only in devices driven to within 5–10 % of their breakdown voltage did we observe local barrier-thickness modulations on the order of 1–2 nm and interface roughening of about 3–4 nm, accompanied by increased diffuse scattering near the top interface but without the formation of new crystalline phases.

These findings collectively address the initial research problem by establishing that nonlinear dc conduction in $SrTiO_3$-based oxide heterostructures arises from a controlled crossover between Ohmic, trap-limited space-charge and Poole–Frenkel-type regimes, with the crossover field and strength of nonlinearity governed by barrier thickness and electrode composition. In practical terms, our data indicate that $SrTiO_3$ thicknesses of 5–10 nm combined with a correlated $La_{0.7}Sr_{0.3}MnO_3$ top electrode yield strong nonlinearity at comparatively modest fields (≈100–200 $kV \cdot cm^{-1}$) while maintaining structural integrity, suggesting these configurations as promising candidates for selector-like elements and leakage-limiting layers in oxide electronics.

The present study is limited to $SrTiO_3$-based heterostructures, dc and quasi-static measurements, and a moderate temperature window. Future work should extend this combined transport–structure approach to other perovskite and binary oxides, explore fast-pulse and AC regimes, and correlate nonlinear conduction with noise and relaxation phenomena, in order to build a more complete picture of strong-field transport and reliability in complex oxide heterostructures.

References

[1] J. Boonlakhorn and P. Thongbai, “Dielectric properties, nonlinear electrical response and microstructural evolution of CaCu3Ti4-xSnxO12 ceramics prepared by a double ball-milling process,” *Ceram. Int.*, vol. 46, no. 4, pp. 4952–4958, Mar. 2020, doi: 10.1016/j.ceramint.2019.10.233.

[2] L. Liu *et al.*, “Dielectric and nonlinear current-voltage characteristics of rare-earth doped CaCu3Ti4O12 ceramics,” *J. Appl. Phys.*, vol. 110, no. 9, Nov. 2011, doi: 10.1063/1.3658258.

[3] C. R. Foschini, R. Tararam, A. Z. Simões, M. Cilense, E. Longo, and J. A. Varela, “CaCu3Ti4O12 thin films with non-linear resistivity deposited by RF-sputtering,” *J. Alloys Compd.*, vol. 574, pp. 604–608, 2013, doi: 10.1016/j.jallcom.2013.05.216.

[4] S. A. Mojarad *et al.*, “A comprehensive study on the leakage current mechanisms of Pt/SrTiO 3/Pt capacitor,” *J. Appl. Phys.*, vol. 111, no. 1, Jan. 2012, doi: 10.1063/1.3673574/927851.

[5] D. Miron, I. Krylov, M. Baskin, E. Yalon, and L. Kornblum, “Understanding leakage currents through Al2O3 on SrTiO3,” *J. Appl. Phys.*, vol. 126, no. 18, Nov. 2019, doi: 10.1063/1.5119703.

[6] S. Boyeras Baldomá *et al.*, “Wear-out and breakdown of Ta2O5/Nb:SrTiO3 stacks,” *Solid. State. Electron.*, vol. 198, Dec. 2022, doi: 10.1016/j.sse.2022.108462.

[7] J. S. Kim *et al.*, “Nonlinear Hall effect and multichannel conduction in LaTiO 3/SrTiO3 superlattices,” *Phys. Rev. B - Condens. Matter Mater. Phys.*, vol. 82, no. 20, Nov. 2010, doi: 10.1103/PhysRevB.82.201407.

[8] H. Leng *et al.*, “Competing conduction mechanisms for two-dimensional electron gas at LaTiO3/SrTiO3 heterointerfaces,” *Appl. Phys. Lett.*, vol. 124, no. 18, Apr. 2024, doi: 10.1063/5.0202403.

[9] J. G. Connell, J. Nichols, J. H. Gruenewald, D. W. Kim, and S. S. A. Seo, “Conducting LaAlO3/SrTiO3 heterointerfaces on atomically-flat substrates prepared by deionized-water,” *Sci. Rep.*, vol. 6, Apr. 2016, doi: 10.1038/srep23621.

[10] C. Yin, K. Prateek, W. Gelling, and J. Aarts, “Tunable Magnetic Scattering Effects at the LaAlO3/SrTiO3Interface by Ionic Liquid Gating,” *ACS Appl. Electron. Mater.*, vol. 2, no. 12, pp. 3837–3842, Dec. 2020, doi: 10.1021/acsaelm.0c00654.

[11] C. Funck and S. Menzel, “Comprehensive Model of Electron Conduction in Oxide-Based Memristive Devices,” *ACS Appl. Electron. Mater.*, vol. 3, no. 9, pp. 3674–3692, Sep. 2021, doi: 10.1021/acsaelm.1c00398.

[12] Y. Zhang *et al.*, “Leakage current characteristics of SrTiO3/LaNiO3/Ba0.67Sr0.33TiO3/SrTiO3 heterostructure

thin films," *Rare Met.*, vol. 40, no. 4, pp. 961–967, Apr. 2021, doi: 10.1007/s12598-020-01497-z.
[13] A. Gómez *et al.*, "Electric and Mechanical Switching of Ferroelectric and Resistive States in Semiconducting BaTiO3– δ Films on Silicon," *Small*, vol. 13, no. 39, Oct. 2017, doi: 10.1002/smll.201701614.
[14] R. Buzio and A. Gerbi, "Resistive switching suppression in metal/Nb:SrTiO3 Schottky contacts prepared by room-temperature pulsed laser deposition," *J. Phys. D. Appl. Phys.*, vol. 57, no. 39, Oct. 2024, doi: 10.1088/1361-6463/ad5c77.
[15] Z. Hu *et al.*, "Ferroelectric memristor based on Pt/BiFeO3/Nb-doped SrTiO 3 heterostructure," *Appl. Phys. Lett.*, vol. 102, no. 10, Mar. 2013, doi: 10.1063/1.4795145.

Information about authors:
Ruslan Kalibek – Master Student, Faculty of Engineering, Süleyman Demirel University, 1/1 Almatinskaya st., Almaty, Kazakhstan, rus.kalibek@bk.ru
Daria Sopyryaeva – MSc, Academic Associate, Institute of Physics, Technical University of Berlin, 17 Straße des, Berlin, Germany, dsopyryaeva@mail.ru

Author Contributions:
Ruslan Kalibek – concept, methodology, resources, data collection, visualization, interpretation, drafting, funding acquisition.
Daria Sopyryaeva – testing, modeling, analysis, editing.

Conflict of Interest: The authors declare no conflict of interest.

Use of Artificial Intelligence (AI): The authors declare that AI was not used.

Received: 22.10.2025
Revised: 14.12.2025
Accepted: 20.12.2025
Published: 23.12.2025